3D Transient Modeling of Bulk High Temperature Superconducting Material in Passive Magnetic Bearing Applications

Dr. Sid Pratap *Senior Member IEEE*, Dr. Clay Hearn

***Abstract*— Bulk high temperature superconductors (HTSC) are being considered for use in several engineering applications including passive magnetic bearings. These bearings besides being passive i.e. inherently stable also offer the promise of lower bearing losses thus they are being considered for use with flywheels for energy storage in applications related to frequency regulation and for correcting forecasting errors associated with renewable energy sources. The effort presented in this paper was undertaken to characterize the performance of these bearings such as longitudinal and transverse stiffness and loss characteristics. To this end, a finite element method using the T-Ω potentials was used for the formulation. The results of the finite element method (FEM) were verified with experiments. These experiments are described. This FEM tool was also used to guide the development of a reduced order model which could run faster and therefore could be used in larger system simulations. Some discussions about the run time on a desktop PC are also presented.**

***Index Terms*—Bulk high temperature superconductors, 3 dimensional, finite element method, transient solution, experimental verification, T-omega method, magnetic bearings, longitudinal and transverse stiffness.**

I. Introduction

PASSIVE magnetic bearings using bulk high temperature superconductors have been researched for a long time. Several topological variants of HTSC passive magnetic bearings designs have been described by Krabbes et al [1]. Starsik et al [2] present the results of testing a flywheel energy storage system using the bulk HTSC bearings. Their results show successful passive operation of the bearings and an integrated flywheel motor/generator operating with very low standby losses. Similarly other flywheel energy systems using bulk HTSC material bearings are described in [3]-[5]. Several of these researchers have tested the systems and report successful operation, however, very little work has been done in modeling the system in an attempt to predict the behavior of the HTSC/PM bearing system. Reference [6] discusses measuring the vertical and lateral forces between a bulk HTSC slab and a permanent magnet. This reference also discusses theoretical calculation based on the frozen image method [7]. However, the frozen image method ignores effects related to the critical current density in the HTSC and therefore has only limited use. There has been, however, a considerable effort in the 2D and 3D modeling of the HTSC superconducting wire [8], [9] and to simulate the activation process in a bulk HTSC [9], [10]. Reference [8] gives a broad comparison of the 2D and 3D finite element methods to model HTSC using the commonly used potential formulation such as (i) the magnetic vector potential and the electric scalar potential (**A**-V, **A** method) and (ii) the magnetic scalar potential and the electric vector potential (**T**-Ω method). Due to the highly non-linear relation (Ohm's Law) between the electric field and the current density in the superconducting material [8] cites assured convergence with the **T**-Ω method. This is also consistent with the authors experience with the 3D, **A**-V, **A** formulation and the **T**-Ω formulations. Therefore the **T**-Ω method was adopted for the formulation in this application. The **T**-Ω method is described in [11], [12].

In what follows the implementation of the **T**-Ω method for this non-linear conductivity problem is described along with the solution method. Thereafter the experimental setup is described for measurement of lateral and the longitudinal stiffness of the permanent magnet/HTSC bearing system. The results are also obtained analytically with the finite element method described here. A comparison of the analytical and experimental results are also presented.

This FEM method was setup to form a basis of comparison in the process of development of a reduced order model which is described in [13]. The reduced order model which has fewer degrees of freedom can be used to model a rotor/bearing system. The main impetus in development of the reduced order model was to speed up the simulation.

II. Governing Equations and the Finite Element Formulation

A. Governing Equations

Maxwell's equations in the quasi-static regime describe the diffusion of the magnetic field into the HTSC material in the time domain. For completeness they are repeated here in equations (1a)-(1d). These equations together with the

This paragraph of the first footnote will contain the date on which you submitted your paper for review. This work was supported by the Stanford University through their Global Climate Energy Project.

S. B. Pratap (email: s.pratap@cem.utexas.edu) and C. S. Hearn (email: hearn@cem.utexas.edu) are with the Center for Electromechanics, University of Texas at Austin, Austin, Texas, 78712 USA.

constitutive relations given in (2a) and (2b) need to be solved

$$\nabla \times \mathbf{H} = \mathbf{J} \tag{1a}$$

$$\nabla \times \mathbf{E} = -\frac{\partial \mathbf{B}}{\partial t} \tag{1b}$$

$$\nabla \cdot \mathbf{B} = \mathbf{0} \tag{1c}$$

$$\nabla \cdot \mathbf{J} = \mathbf{0} \tag{1d}$$

with the appropriate boundary conditions.

$$\mathbf{B} = \mu \mathbf{H} \tag{2a}$$

$$\mathbf{J} = \sigma(|\mathbf{J}|)\mathbf{E} \tag{2b}$$

Here 'μ' is the magnetic permeability and 'σ' is the electrical conductivity and in the HTSC it is a function of the magnitude of the current density in the superconductor.

The non-linearity in the solution of these equations comes from (2b) which indicates that the conductivity is a function of the current density. This relation between the current density and the electric field can best be described by equation 3 and Fig. 1.

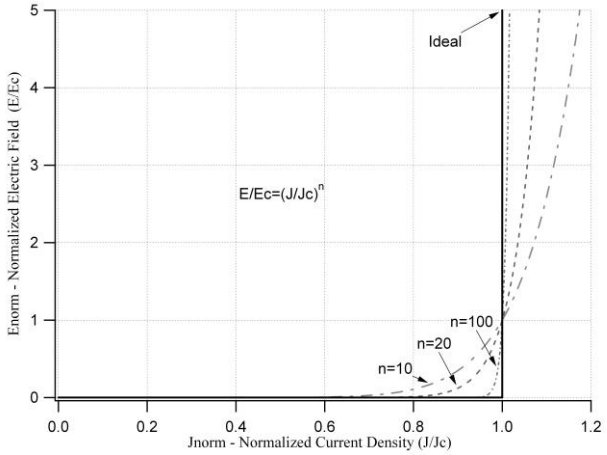

Figure 1: The Ohm's Law for HTSC material - conductivity is dependent on the current density thus making the problem non-linear

$$\frac{|\mathbf{E}|}{E_c} = \left(\frac{|\mathbf{J}|}{J_c}\right)^n \tag{3}$$

Here' J_c' is the critical current density of the material and it depends on the type of material e.g. YBCO, MgB_2, etc. and the pinning technique. It is also dependent on the temperature and weakly on the magnetic field. Values can range from a few kA/cm^2 to a few 100 kA/cm^2. 'E_c' is the electric field at the critical current density and it is for most all materials in the range of 1 μV/cm. The index 'n' is also dependent on the material.

B. Potential Formulation

The total field is divided into two components and solved for separately. One component corresponds to the externally applied field ($\mathbf{H_0}$) i.e. through a current in a coil or from permanent magnets in the absence of the superconductor and the other component ($\mathbf{H_i}$) corresponds to the induced currents in the conductive material.

$$\mathbf{H} = \mathbf{H}_0 + \mathbf{H}_i \tag{4}$$

'$\mathbf{H_0}$' i.e. the source field in the absence of the HTSC can be solved for separately, a priori. A variety of different formulations can be used to do this. This source field '$\mathbf{H_0}$' in some cases may even be obtained simply using the Biot-Savart Law. Then what remains to be solved is simply the field in the three regions of Fig. 2 due to the induced eddy currents in the HTSC ('$\mathbf{H_i}$') and the total field can be recovered by superposition. Since superposition is used one is restricted to linear magnetic materials. This is not a significant restriction for the present task.

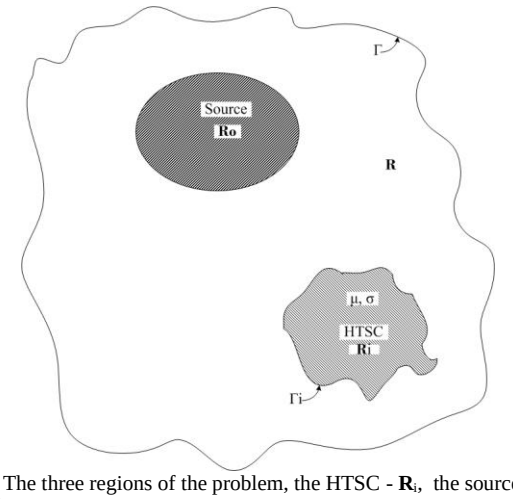

Figure 2: The three regions of the problem, the HTSC - $\mathbf{R_i}$, the source of the external field - $\mathbf{R_o}$, and the region in between - mostly air - $\mathbf{R}$

$$\nabla \times \mathbf{H}_i = \mathbf{0} \quad \text{in regions '}\mathbf{R}\text{' and '}\mathbf{R}_0\text{'} \tag{5}$$

Here use is made of the fact that the source field satisfies the following equations.

$$\nabla \times \mathbf{H}_0 = \mathbf{J}_0 \quad \text{in region } \mathbf{R}_0 \tag{6}$$

$$\nabla \times \mathbf{H}_0 = \mathbf{0} \quad \text{in region } \mathbf{R} \text{ and } \mathbf{R}_i \tag{7}$$

Therefore the magnetic field intensity '$\mathbf{H}_i$' can be represented by the gradient of a scalar potential 'Ω'.

$$\mathbf{H}_i = -\nabla\Omega \quad \text{in regions '}\mathbf{R}\text{' and '}\mathbf{R}_0\text{'} \tag{8}$$

In region $\mathbf{R_i}$, using (7) we get,

$$\nabla \times \mathbf{H}_i = \mathbf{J}_i \tag{9}$$

Now since we are in the quasi-static regime we use (1d) $\nabla \cdot \mathbf{J}_i = \mathbf{0}$, so that we can represent the current density as the curl of a vector potential i.e. the electric vector potential $\mathbf{T}$.

$$\mathbf{J}_i = \nabla \times \mathbf{T} \tag{10}$$

Combining (9) and (10) we can write,

$$\mathbf{H}_i = \mathbf{T} - \nabla\Omega \tag{11}$$

In the last step we apply Faraday's law by substituting (2b), (4), (7) and (11) in (1b) this gives,

$$\nabla \times \rho(|\mathbf{J}_i|)\nabla \times \mathbf{T}_i + \mu_0 \frac{\partial(\mathbf{T} - \nabla\Omega)}{\partial t} = -\mu_0 \frac{\partial \mathbf{H}_0}{\partial t} \tag{12}$$

Here use is made of the relation ρ=1/σ, where ' ρ ' is the resistivity of the material as obtained from Fig. 1. In this equation the time rate of change of the external field '$\mathbf{H_0}$' acts as the source term for equation 12.

One more equation needed in the HTSC region '$\mathbf{R}_i$' can be obtained by substituting (2a) and (11) in (1c).

$$\nabla \cdot \mu\left(\mathbf{T} - \nabla\Omega\right) = 0 \tag{13}$$

Equations (12) and (13) will result in symmetric terms in the stiffness matrix when the equations are discretized by the Galerkin method. Since so far only the curl of the vector potential **T** has been defined for uniqueness it is necessary that the divergence is also defined. The coulomb gauge i.e. $\nabla \cdot \mathbf{T} = \mathbf{0}$ was enforced using the method of Lagrangian multipliers. However, it was found that unique solutions were also obtained if this gauge was not enforced. This observation was also made by Biddlecombe et al [14], Trowbridge [15] with the **T**-Ω formulation.

In the regions excluding the HTSC i.e. **R** and $\mathbf{R_0}$, there is only one unknown that needs to be solved i.e. Ω which from equation (1c) and (8) gives the Laplacian:

$$\nabla^2\Omega = 0 \tag{14}$$

With the T-Ω formulation it is necessary that the conductive region with eddy currents be simply connected. The work around for the case of a multiply connected eddy current region is to use a very low conductivity in the hole through the region [16]. At the boundary of the eddy current region $\mathbf{R}_i$ it is necessary that the condition, $\mathbf{J} \cdot \mathbf{n} = 0$, be satisfied. That leads to the boundary condition $\mathbf{T} \times \mathbf{n} = \mathbf{0}$ or the tangential component of the electric scalar potential vanishes on that surface. This is fairly easy to implement when the surfaces are aligned with the coordinate system, however, its implementation for general surfaces and curved surfaces need special attention. There are variety of methods to deal with the general boundary. One method, suggested by Rodger [17] transforms to the local coordinates and uses local variables. For the work presented here the global coordinates were used and the boundary conditions were expressions involving direction cosines and a combination of global variables which were enforced with Lagrangian multipliers.

C. Finite Element Implementation

The unknowns in region $\mathbf{R_i}$ are the magnetic scalar potential Ω and the three components of the electric vector potential; T_x, T_y, and T_z. Additional degrees of freedom are included for the Lagrangian multipliers at the boundary nodes. In regions $\mathbf{R_0}$ and **R** the only unknown is the magnetic scalar potential Ω.

The stiffness matrix is obtained by the Galerkin method by applying the appropriate weighting functions to equations (12), (13) and (14) and integrating over the domains. The expressions for the various stiffness terms are fairly elaborate and therefore have not been presented here. Since the problem is non-linear an iterative solution is obtained using the Newton-Raphson method. For this the tangent stiffness matrix is calculated from the stiffness matrix. Several terms of the stiffness matrix have the resistivity of the HTSC in them which is dependent on the current density and therefore the unknowns T_x , T_y and T_z. Iterations yield the values of improvements to the unknowns which are then added to the previous approximations of the unknowns. The tangent stiffness matrix is then updated for the next iteration. One could perform iterations without updating the tangent stiffness matrix as is done in the modified Newton Raphson method, however, considering that the solution time is significantly more than the time to calculate the stiffness matrix, the update of the values is necessary to minimize the number of iterations. The direct solver as opposed to an iterative solver is used since the problem is non-linear, which increases the chance of converging. The iterations are concluded once the changes in the potentials are less than 0.1%.

The direct solver used is a frontal solver [18] that minimizes the storage requirements.

III. EXPERIMENTAL SETUP

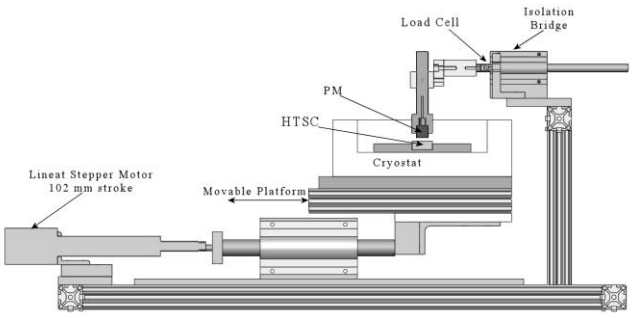

Figure 3: Experimental setup to measure the horizontal forces between a PM and an HTSC disc under the transverse motion of the HTSC after field cooling

Fig. 3 shows the experimental setup to measure the force in the horizontal direction on the PM due to the transverse (left-right) motion of the HTSC. The particulars of the HTSC disc and the PM cylinder are as shown in table 1.

TABLE I
HTSC AND PM SPECIFICS

Part	Parameter	Units	Value
HTSC	Material	YBCO	-
	Critical Current Density (Jc)	kA/cm^2	9
	Diameter	mm.	47
	Height	mm.	15
PM	Material	NdBFe (N48)	-
	Peak Surface Field	T	0.4T at 77K*
	Diameter	mm.	19
	Height	mm.	6.4

* Since the strength of a neodymium magnet can decrease by about 15% at cryogenic temperatures compared to room temperature

The Bulk HTSC disc was glued in the recess made in the G10 plate in the cryostat (Styrofoam). The G10 plate was clamped at two locations to the cryostat. The cryostat was fastened on a movable platform which was connected through rods on linear bearings to a linear stepper motor with a 102 mm. stroke capability. The PM was mounted at the end of a G10 rod, and was placed so that its lower surface was 2mm above the surface of the HTSC with their centers as closely aligned as possible. The HTSC disc was field cooled in the presence of the PM. The horizontal force on the PM was measured by a load cell and it was recorded as a function of time. The linear motor moved the entire platform assembly ±20mm and ±10 mm. at a constant speed over a period of 30 seconds.

Fig. 4 shows the setup to measure the vertical force under the transverse motion of the HTSC. The only part that is different is the placement of the load cell therefore figure 4

only shows that part. The rest of the setup is as in figure 3. For clarity a photograph of the setup for the vertical force measurement is also shown (figure 5).

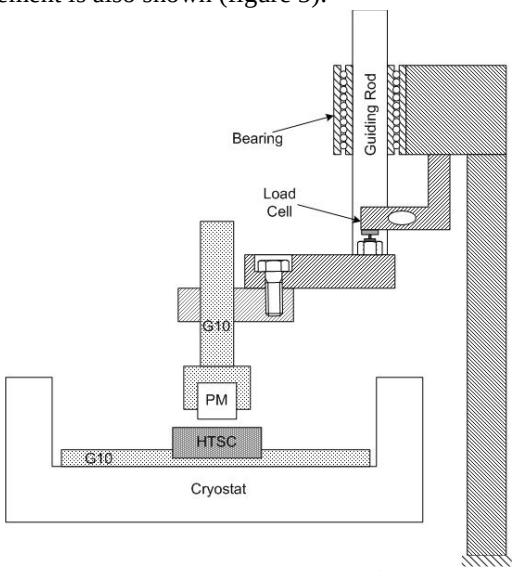

Figure 4: Experimental setup to measure the vertical forces between a PM and an HTSC disc under the transverse motion of the HTSC after field cooling

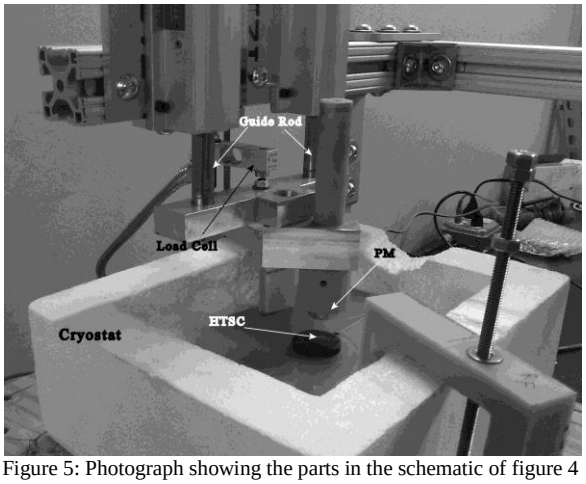

Figure 5: Photograph showing the parts in the schematic of figure 4

Table 2 give the specifics of the load cells used for the two measurement setups. These load cells were calibrated against known weights prior to collecting data under transverse motion of the HTSC. Data collected is shown in figures 11-14 alongside the results of the finite element analysis.

TABLE II
LOAD CELL INFORMATION

Test	Make/Model	Capacity (N)	Sensitivity (N/V)
Horizontal Force	Omega LCL-005	22	19.113
Vertical Force	Phidget - CZL635	49	46.637

IV. FINITE ELEMENT MODEL

To duplicate the test in a finite element model is fairly straightforward. It only involves two components and the surrounding air. Use is made of the symmetry plane as shown in figure 6. This allows one to model half the geometry.

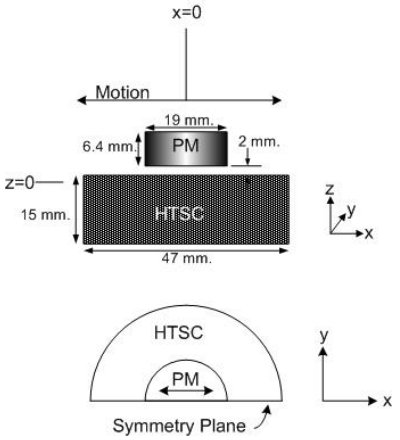

Figure 6: Geometry for the finite element model showing the symmetry plane.

Based on the discussions presented in section II on the potential formulations the field produced by the magnet (external field $\mathbf{H_o}$) provides the source term for equation (12). This can be calculated a priori without modeling the HTSC. Closed form expressions were used to calculate the field in the entire volume of the finite element model - Fig 7. For more complicated geometries where closed form solutions would be difficult to obtain one can calculate the fields produced by the source using FEM and then using interpolation where needed.

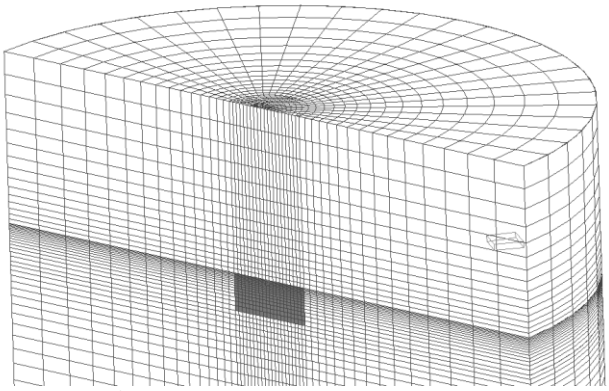

Figure 7: 3D finite element geometry showing the HTSC disk and the surrounding air

The external field, for the present problem, was calculated for each time step and correspondingly each position of the magnet. For the purpose of determining the eddy current density in the HTSC and the forces one only needs to calculate the external field in the region of the HTSC. However to enable the imaging of the total field in the entire region it was necessary to calculate it at all the nodes of figure 7. The time derivative required in equation (12) at the integration points of the elements of the HTSC was obtained by taking the finite difference time derivative as the PM was moved.

The FEM model had about 26,500 nodes and about 24,000 elements. The total no. of degrees of freedom that were being solved, including the Lagrangian multipliers for the constraints, were about 37,000. This model was run on a PC with a 64-bit operating system with an Intel Xeon CPU at 3 GHz. The PC had only 8 GB RAM. The model was run with various time steps over the 30 second interval, Δt=0.75 s (41

steps), Δt=0.375 s (81 steps) and Δt=0.1875 s (161 steps). The run time versus the time step is shown in figure 8. The run time does not double when the time step is halved because the

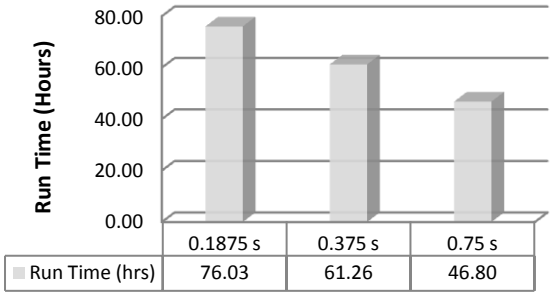

Figure 8: Run time versus the time step for the

convergence is obtained with fewer iterations with the smaller time step. Nominally the time per iteration is 295 s or about 5 minutes. There are also small changes in the force versus position profile as the time step is changed. The largest difference is seen in going from 0.75 s to 0.375 s. Figure 9 shows the force profile for the force in the direction of the motion. The arrows indicate whether the distance is increasing or decreasing. The forces are restoring in nature i.e. in a direction to reduce the separation of the centers of the two parts. It also exhibits the classical hysteresis seen in the superconductors. As the PM moves relative to the HTSC there is some local saturation of the current density, allowing penetration of the field. This field is then trapped in that region of the HTSC and therefore modifies the force on the way back. If the oscillations were

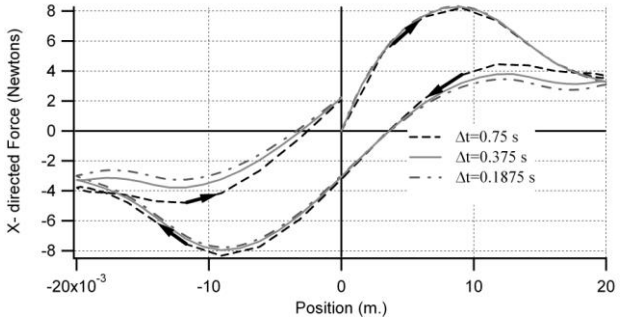

Figure 9: Restoring force versus separation of the centers of the PM and HTSC - exhibits the hysteresis typical of superconductors

to continue then the area enclosed by the curve is the loss per cycle that one would observe in the superconductor. In this case the loss per cycle is approximately 0.15 Joules with a 20 mm. displacement. The excursions around the center for an actual bearing application would be relatively small and the losses much lower correspondingly.

There is also another force that acts on the PM that is in the vertical direction(z-directed) away from HTSC (repulsive). This happens because as the PM moves from its initial location, the HTSC responds to exclude the fields from the interior of the conductor. This compressed flux is tangential to the HTSC surface and results in a repulsive force. This repulsive force is not equally distributed around the PM because part of the PM sees new material and part sees an area where there already is a trapped field from the zero field cooling. This will result in the oscillations of the magnet axis. When considering passive magnetic bearings this must be born in mind as it couples oscillations in one plane to that in the other plane. Figure 10 shows the net vertical force for the same conditions as in figure 9. The force is seen to drop beyond about 14 mm because part of the magnet has now moved past the edge of the HTSC.

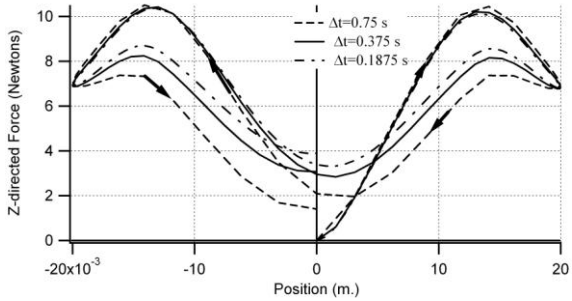

Figure 10: Repulsive force versus separation of the centers of the PM and HTSC - also shows hysteresis

V. Comparison of Results from Experiments and FEM

In this section a comparisons of the results from the FEM analysis and the experimental observations are made. The experimental setup has been described in section 3.

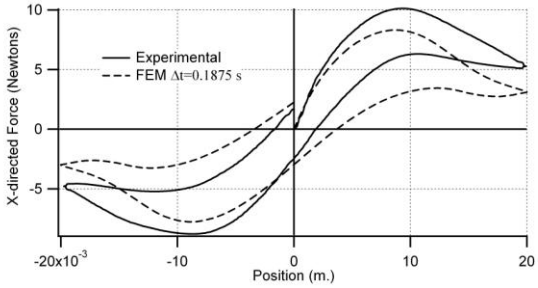

Figure 11: Comparison of the restoring force (x-directed) from Experiment and FEM analysis for ± 20 mm. motion

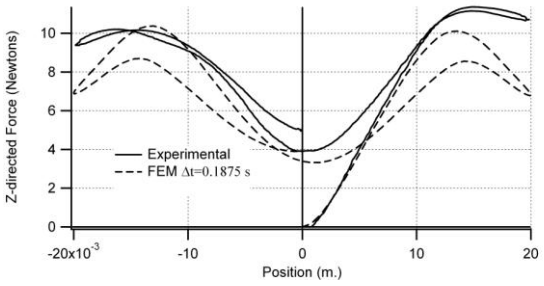

Figure 12: Comparison of the repulsive force (z-directed) from Experiment and FEM analysis for ± 20 mm. motion

Considering figures 11-14 for restoring and repulsive forces and for the 10 mm. and 20 mm. displacements it is observed that the forces compare well in general as far as magnitude and general shape are concerned. Some differences remain however. In general the experimental forces obtained are slightly higher than the FEM analysis. Also note that the area enclosed under the hysteresis curve is larger than the experimental observation for the vertical force in figures 12

and 14. It is likely that the current density we have assumed (9 kA/cm^2) in our analysis may in fact be somewhat higher. another point where it may be necessary to tweak is the index 'n' in (3) which we have assumed as n=11.

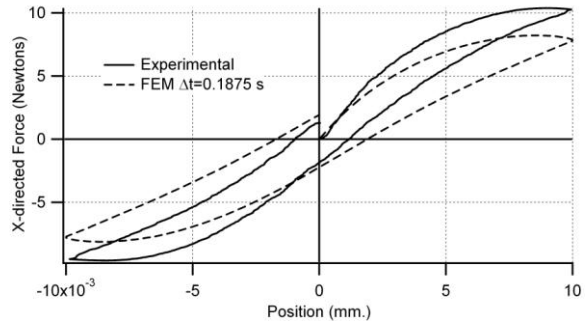

Figure 13: Comparison of the restoring force (x-directed) from Experiment and FEM analysis for ± 10 mm. motion

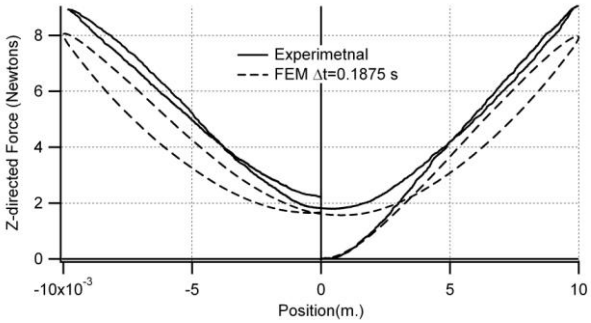

Figure 14: Comparison of the repulsive force (z-directed) from Experiment and FEM analysis for ± 10 mm. motion

VI. Conclusion

A finite element method has been presented that works fairly well in modeling bulk high temperature superconducting material. This method is quite robust and converges to a solution despite the non-linearity in the material resistivity. The experimental setup has been described and the results of the finite element analysis have been compared to the experimental observations. They are in fairly good agreement as regards magnitude and trends.

This code can be used to study more elaborate arrangements for passive magnet bearing applications. This code could also be used for the dynamic study of the behavior of a rotor suspended using PMs and HTSCs

Acknowledgment

The author would like to thank the Global Climate Energy Project at the Stanford University for funding the work presented here.

References

[1] G. Krabbes, G. Fuchs, W.-R. Canders, H.May and R.Palka, "High Temperature Superconductor Bulk Materials," *Wiley-VCH*, 2006, Ch. 11, pp. 199–258, 2006.

[2] M. Strasik, P. E. Johnson, A. C. Day, J. Mittleider, M. D. Higgins, J. Edwards, J. R. Schindler, K. E. McCrary, C. R. McIver, D. Carlson, J. F. Gonder, and J. R. Hull, "Design, Fabrication, and Test of a 5-kWh/100-kW Flywheel Energy Storage Utilizing a High-Temperature Superconducting Bearing", *IEEE Transactions on Applied Superconductivity*, Vol. 17, No. 2, pp. 2133-2137, June 2007.

[3] S O Siems, W-R Canders, H Walter and J Bock, "Superconducting magnetic bearings for a 2 MW/10 kWh class energy storage flywheel system", "*Superconductor Science and Technology*, Vol. 17, pp S229-S233, 2004.

[4] Thomas M. Mulcahy, John R. Hull, Kenneth L. Uherka, Robert G. Abboud, and John J. Juna, "Test Results of 2-kWh Flywheel Using Passive PM and HTS Bearings", IEEE Transactions on Applied Superconductivity, Vol. 1 I, No. 1, pp 1729-1732, March 2001.

[5] H. Teschima, T. Tawara, J. Kobuchi, T. Suzuki, R. Shimada, "Ring-Shaped Flywheel Energy Storage Systems with Superconducting Levitation", *Proceedings of the Power Conversion Conference - Nagakoa 1997*, Vol. 2, pp 701-706, Conference dates 3-6 August 1997.

[6] J. R. Hull and A. Cansiz, " Vertical and lateral forces between a permanent magnet and a high temperature superconductor", *J. Appl. Phys.*, Vol. 86, No. 11, pp 6396-6404, 1999

[7] A.A. Kordyuk, "Magnetic levitation for hard superconductors", *J. Appl. Phys.*, Vol. 83, No. 1, pp 610-612, 1998

[8] F. Grilli, S. Stavrev, Y. Le Floch, M. Costa-Bouzo, E. Vinot, I. Klutsch, G. Meunier, P. Tixador, and B. Dutoit "Finite-Element Method Modeling of Superconductors: From 2-D to 3-D", *IEEE Transactions on Applied Superconductivity*, Vol. 15, No. 1, pp. 17-25, March 2005.

[9] D. Ruiz-Alonso, T. A. Coombs, and A. M. Campbell, "Numerical Analysis of High-Temperature Superconductors With the Critical-State Model", *IEEE Transactions on Superconductivity*, Vol. 14, No. 4, pp 2053-2063, December 2004.

[10] H. Ohsaki, T. Shimosaki and N. Nozawa, "Pulse field magnetization of a ring-shaped bulk superconductor", *Superconductor Science and Technology*, Vol. 15, pp 754-758, 2002.

[11] M.R. Krakowski, "On Certain Properties of the Electric Vector Potential in Eddy Current Problems", IEE Proceedings Vol. 132, Pt. A, No. 7, pp 445-449, November 1985.

[12] T.W. Preston, A.B.J. Reece, Solution of 3-Dimensional Eddy Current Problems: The T-Ω method", *IEEE Transactions on Magnetics*, Vol. 18, No. 2 , pp 486-491, March 1982.

[13] C.S. Hearn, S. B. Pratap, D.Chen, R. G. Longoria, "Lumped Parameter Model to Describe Dynamic Translational Interaction for High temperature Superconducting Bearings", Accepted for publication in the *IEEE Transactions on Superconductivity*.

[14] C.S. Biddlecombe, E.A. Heighway, J. Simkin, C.W. Trowbridge, "Methods for Eddy Current Computation in Three Dimensions", *IEEE Transactions on Magnetics*, Vol. 18, No. 2, pp. 492-497., pp. 173-180, March 1982.

[15] C.W. Trowbridge, "Some Three Dimensional Eddy Current Algorithms under Investigation in UK", *Computational Electromagnetics - IMACS*, editor Z.J. Cendes, Elsevier Science Publishers B.V., pp. 173-180, 1986

[16] T. Nakata, N. Takahashi, K. Fujiwara, Y. Okada, "Improvements of the T- Ω Method for 3-D Eddy Current Analysis", *IEEE Transactions on Magnetics*, Vol. 24, pp. 94-97, 1988.

[17] D. Rodger, J.F. Eastham, " The use of transformations in applying boundary conditions to three-dimensional vector field problems", *IEE Proceedings*, VOl 132, Pt. A, No. 4, July 1985.

[18] Irons, B. M., "A frontal solution scheme for finite element analysis. Int. J. Numer. Methods Eng. Vol. 2, pp. 5-32, 1970.

Dr. Siddharth Pratap (M'88-SM'10) received the BS in electrical engineering from the University of Bombay, Bombay, India in 1979, the MS in electrical engineering from the University of Texas at Austin in 1982, and the PhD in electrical engineering from the University of Texas at Austin in 1996 in the area of power systems and electromagnetics. His research specialty is in the area of electromechanics, computational electromagnetics, and transients in pulsed electrical

equipment. He has expertise in the design, analysis, simulation, and experimental performance assessment of electromechanical devices such as linear electrical motors, high average power electrical machines, and pulsed power equipment.

Dr. Pratap served on the integrated product team in the design of the linear induction motor for the Navy's EMALS (Electromagnetic Aircraft Launch System) which is currently being tested and mounted on the next generation of aircraft carriers. He has also worked on the design and analysis of magnetic levitation transportation systems. Recently he has been involved in developing compact, high power systems for mobile Navy and Air Force applications. He also develops 2D and 3D finite element analysis codes to perform transient and steady state, electromagnetic, electrostatic, and thermal analysis on electromechanical equipment including superconducting materials.

Dr. Clay S. Hearn obtained his BS and MS degrees in mechanical engineering from the University of Texas at Austin in 2001 and 2008, respectively. In August of 2013, he finished his Ph.D. in mechanical engineering from the University of Texas with a focus on dynamic system modeling and controls.

Mr. Hearn has been a Research Engineer at the Center for Electromechanics at the University of Texas at Austin since 2002. His work has focused on modeling, analysis, and control of energy storage for various applications, including hybrid vehicles, grid utilities, renewable energies, and pulsed power. He has employed dynamic modeling and control techniques to access potential performance improvements for heavy hybrid vehicles, marine, and microgrid applications by evaluating the addition of energy storage options, including flywheels, lithium ion batteries, and ultracapacitors. Mr. Hearn has also worked extensively on design and evaluation of hydrogen fueled vehicles. Additional work has included FEA structural and thermal modeling and analysis for high-speed composite flywheel energy storage systems and pulse power alternators.